

On-surface synthesis and characterization of individual polyacetylene chains

Shiyong Wang^{1,2,6}, Qiang Sun^{3,6}, Oliver Gröning¹, Roland Widmer¹, Carlo A. Pignedoli¹, Liangliang Cai³, Xin Yu³, Bingkai Yuan², Can Li², Huanxin Ju⁴, Junfa Zhu⁴, Pascal Ruffieux¹, Roman Fasel^{1,5*} and Wei Xu^{3*}

Polyacetylene (PA) comprises one-dimensional chains of sp^2 -hybridized carbon atoms that may take a *cis* or *trans* configuration. Owing to its simple chemical structure and exceptional electronic properties, PA is an ideal system to understand the nature of charge transport in conducting polymers. Here, we report the on-surface synthesis of both *cis*- and *trans*-PA chains and their atomic-scale characterization. The structure of individual PA chains was imaged by non-contact atomic force microscopy, which confirmed the formation of PA by resolving single chemical bond units. Angle-resolved photoemission spectroscopy suggests a semiconductor-to-metal transition through doping-induced suppression of the Peierls bond alternation of *trans*-PA on Cu(110). Electronically decoupled *trans*-PAs exhibit a band gap of 2.4 eV following copper oxide intercalation. Our study provides a platform for studying individual PA chains in real and reciprocal space, which may be further extended to study the intrinsic properties of non-linear excitons in conducting polymers.

Polyacetylene (PA)—a chain of carbon atoms with alternating single and double bonds in either a *cis* or *trans* geometry—was recognized as the first conducting polymer in 1976, leading to the development of the field of organic conducting polymers^{1–4}. Its unusual electronic, magnetic and optical properties^{5–16} derive from the fact that *trans*-PA hosts degenerate ground-state configurations, resulting in different phases of bond alternations between the single and double C–C bonds. At a domain wall, a new type of excitation (also known as a soliton) exists and a zero-energy electronic state is created according to the Su–Schrieffer–Heeger model^{17,18}. The electrical conductivity of PA can be tuned over the full range (from semiconductor to metal) through doping^{1,7,12}. At a high dopant concentration, calculations predict energy gap closure through suppression of the bond alternation of pristine *trans*-PA^{19,20}. Despite the fact that PA and its derivatives have been extensively studied by many conventional techniques through collecting average signals on an ensemble of PA samples, the synthesis of clean, individual PA chains—and structural and electronic characterization—has remained elusive, leaving some crucial questions unanswered. In particular, the formation mechanism and nature of solitons have not been studied in real space due to limited spatial resolution^{4,16}.

On-surface synthesis provides a versatile and convenient route for the fabrication of conjugated carbon nanostructures²¹, and allows for real-space characterization by scanning probe microscopies down to the single chemical bond limit. For example, the formation of one-dimensionally aligned alkane chains²², graphene nanoribbons^{23,24} and triangulene molecules²⁵ have recently been reported. Although PA holds a very simple atomic structure and the synthesis of bulk PA has long been developed through conventional chemistry, the on-surface synthesis of PA—particularly of individual PA chains—remains challenging. The most straightforward

way to synthesize PA is through polymerization of acetylene. However, the chemistry of the acetylenic group on surfaces faces various complications, such as thermally induced dehydrogenative homocoupling^{26,27}, dehydrogenative organometallic coupling²⁸ and cyclotrimerization^{29,30}. Although direct polymerization of acetylenic groups is energetically most favourable according to density functional theory (DFT) calculations²⁶, the complications of adsorbate–substrate interactions prohibit such a reaction on most metal substrates. It would thus be of general interest to develop an efficient strategy to the polymerization of acetylenic groups on surfaces.

Here, we show how an on-surface synthesis approach can be developed to fabricate PA chains, especially with the geometrically pure *trans*-form. Scanning tunnelling microscopy/spectroscopy (STM/STS), non-contact atomic force microscopy (nc-AFM), X-ray photoelectron spectroscopy (XPS) and angle-resolved photoemission spectroscopy (ARPES) together with tight-binding and DFT calculations have been used to determine the structural and electronic properties of the PA chains.

Results and discussion

Synthesis and structural characterization. As illustrated in Fig. 1, to facilitate the formation of linearly aligned polymers we chose the anisotropic Cu(110) surface as a template because of its relatively high chemical activity, and one-dimensional (1D) templating due to the close packing of rows along the $[1\bar{1}0]$ direction. The acetylene molecule is selected as the precursor for the fabrication of PAs by on-surface synthesis. To avoid the unwanted dehydrogenative organometallic coupling reported previously²⁸, the key is to dose acetylene molecules onto a Cu(110) surface held at relatively low temperatures considering the lower energy barrier needed for the direct polymerization reaction. Here, we optimized the experimental conditions

¹Empa, Swiss Federal Laboratories for Materials Science and Technology, Dübendorf, Switzerland. ²Key Laboratory of Artificial Structures and Quantum Control, School of physics and Astronomy, Shanghai Jiao Tong University, Shanghai, China. ³Interdisciplinary Materials Research Center, College of Materials Science and Engineering, Tongji University, Shanghai, China. ⁴National Synchrotron Radiation Laboratory, University of Science and Technology of China, Hefei, China. ⁵Department of Chemistry and Biochemistry, University of Bern, Bern, Switzerland. ⁶These authors contributed equally: Shiyong Wang, Qiang Sun. *e-mail: roman.fasel@empa.ch; xuwei@tongji.edu.cn

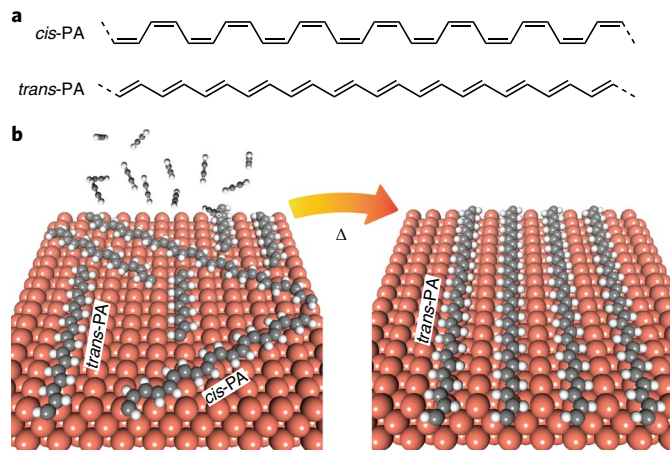


Fig. 1 | A schematic illustration of the on-surface fabrication of PA. a, The chemical structure of *cis*- and *trans*-PA. **b**, A schematic illustration of the formation of mixed *cis*- and *trans*-PA on a Cu(110) substrate (left) and the transformation to *trans*-PA (right) following thermal activation.

and found that the polymerization reaction prevails for substrate temperatures ranging from 300 K to 350 K, and the dehydrogenative organometallic coupling dominates for substrate temperatures above 400 K. Moreover, an earlier spectroscopic study has revealed that acetylene cyclization to benzene over Cu(110) occurs at a very low temperature of 120 K (ref. ³¹, see a detailed summary of the different products in Supplementary Fig. 1).

The reaction temperatures for cyclization, direct polymerization and dehydrogenative organometallic coupling of acetylene molecules on Cu(110) are well separated, allowing for the selective fabrication of PA on this substrate. After dosing acetylene onto the Cu(110) surface, which was held at 300 K and followed by mild annealing to ~ 370 K, meandering 1D chain structures are observed (Fig. 2a). From the close-up STM image shown in Fig. 2b, we can distinguish two types of chain segments with distinct widths and orientations. The ones with the narrower appearance (highlighted by white ellipses) grow straight along the close-packed [110] direction of the substrate, whereas the wider ones (blue ellipses) orient along the [1 $\bar{1}$ 2] direction and the symmetrically equivalent directions of the substrate. To reveal the atomic-scale structure of the chains, we resort to bond-resolved nc-AFM imaging³². The nc-AFM frequency-shift image acquired using a CO-functionalized tip (Fig. 2c) clearly resolves the chemical structure of the chains³². From the high-resolution nc-AFM images in Fig. 2c,d, we are able to assign the wide and narrow segments to *cis*- and *trans*-PA, respectively (see below). As revealed by nc-AFM imaging, *cis*-PA exhibits a chain periodicity of 4.40 ± 0.02 Å, which coincides with the Cu interatomic distance along the [1 $\bar{1}$ 2] direction. Experimental observations are reproduced by DFT calculations, with both the simulated STM image and the lattice constant agreeing well with the experiments (see Fig. 2d). To gain further chemical information on the chain structures, we performed an XPS analysis, which reflects the unsaturated (*sp*- or *sp*²-hybridized) carbon atoms in the chains (see Supplementary Fig. 2)³³.

Interestingly, we observe a *cis*-to-*trans* isomerization at further elevated temperatures. As shown in Fig. 3a, annealing the sample to 470 K gives rise to well-aligned *trans*-PA chains along the [1 $\bar{1}$ 0] direction of the substrate; that is, all of the *cis*-PA chains have been transformed into the *trans* form following thermal treatment. The average length of the *trans*-PA chains is around 5.5 nm, or 45 carbon atoms (see the length distribution in Supplementary Fig. 3), with some chains extending to 50 nm. The nc-AFM frequency shift

image in Fig. 3b clearly reveals the chemical structure of *trans*-PA (with a periodicity of 2.44 ± 0.02 Å along the polymer axis, see Supplementary Fig. 4 for the error estimation). Figure 3c shows the STM image of a longer *trans*-PA chain, in which a moiré pattern is observed due to the lattice mismatch between the Cu substrate (2.56 Å) and the *trans*-PA chain (2.44 Å). For comparison with the experiment, we have performed DFT calculations for an infinitely long *trans*-PA on Cu(110) in a (3 × 4) supercell geometry (Fig. 3b). Although this constrains the PA repeat distance to the Cu–Cu distance of 2.56 Å, it still allows for investigation of the PA/Cu(110) adsorption configuration. The PA chain is located at an adsorption height of 2.1 Å and its carbon backbone is directly above a Cu row of the surface, with alternating C–C bond lengths of 1.38 Å and 1.41 Å. Aside from neglecting the moiré pattern, an STM simulation of the resulting PA/Cu system is found to be in good agreement with the experiment. The DFT calculations for a finite-length, 54-carbon-atom-long *trans*-PA chain on Cu(110) result in a somewhat smaller PA repeat distance of 2.52 Å, but otherwise corroborate the picture obtained from the periodic calculation (see Supplementary Fig. 5).

Our established on-surface synthesis strategy shares similarities with its solution-based counterpart regarding the *cis* to *trans* isomerization. The first solution-based polymerization of acetylene was reported by Natta et al. in 1958, who found that both *cis*- and *trans*-PA can be selectively obtained by tuning the polymerization temperature³⁴. At a lower temperature of ~ 200 K, they achieved mostly *cis*-PA, which transformed into *trans*-PA following heating to 420 K. It is also known that the polymerization of acetylene yields not only highly polymerized PA, but also benzenes¹⁵. Here, in our study, the 1D constraint of the Cu(110) surface drives the reaction predominantly into straight *trans*-PA, but we notice that some *trans*-PA termini exhibit a ring-like structure reminiscent of benzene or larger rings. Annealing *trans*-PA/Cu(110) samples to a higher temperature of 500 K for 30 min increases the amount of such ring-like termini (see Supplementary Fig. 6).

Electronic properties. The electronic properties of *trans*-PA depend crucially on the C–C bond lengths, which determine the hopping integrals between neighbouring sites in a tight binding picture. The tight binding dispersion relation of the π -bands of *trans*-PA can be determined analytically, which leads to the energy spectrum $E(k) = \pm \sqrt{t_1^2 + t_2^2 + 2t_1 t_2 \cos(ka)}$, where k denotes the wavevector, t_1 (t_2) denotes the hopping integral for single (double) C–C bonds, $-$ ($+$) yields the occupied (empty) band and a is the unit cell length. The energy gap between the occupied and empty bands is $\Delta = 2|t_1 - t_2|$. In the gas phase, given the natural values of $t_1 \approx 2.5$ eV and $t_2 \approx 3.5$ eV, *trans*-PA is a semiconductor with a gap around 2 eV (see the band dispersion in Fig. 4a)¹⁶. In the highly doped regime, the Peierls instability (that is, the bond alternation) is supposed to be suppressed ($t_1 = t_2$) and thus *trans*-PA will become a metal with a zero-energy gap, as shown in Fig. 4b (ref. ¹⁹). Despite the current debate on the existence of bond alternation in PA in the absence of terminal double bond effects³⁵, the following analysis of electronic data will be based on this simple and instructive tight-binding picture.

As can be seen from the STM and AFM images shown in Fig. 3, our samples comprise well-aligned and -separated *trans*-PA chains, which allow for both real- and reciprocal-space characterization of their electronic properties. In particular, the excellent degree of alignment of the *trans*-PA chains along the [1 $\bar{1}$ 0] direction of the Cu(110) substrate allows access to the band dispersion through ARPES. Figure 4c shows a comparison of the experimental ARPES constant-energy (k_x, k_y) maps with tight-binding-simulated ones. These ARPES maps display the photoemission intensity of the *trans*-PA-covered Cu(110) after subtraction of a map of one of the clean Cu(110) substrates (see the individual maps in

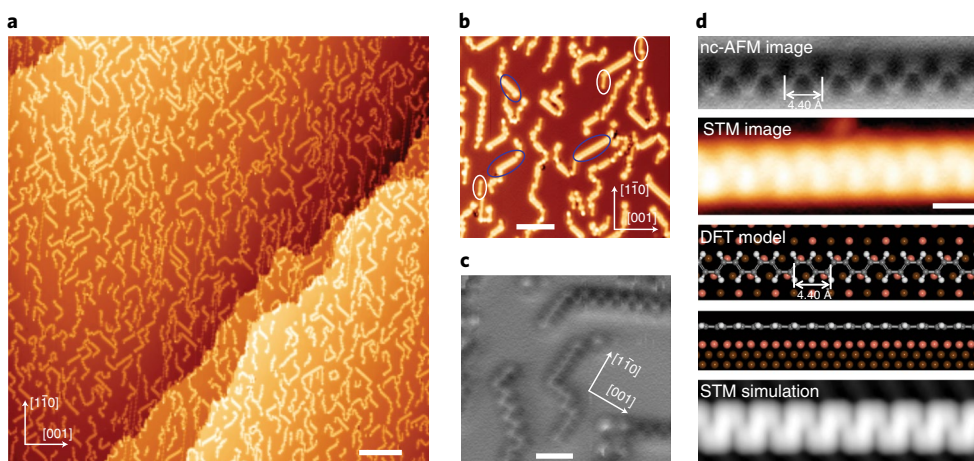


Fig. 2 | The structural properties of *cis*-PA. **a**, A large-scale STM image (bias voltage, 70 mV; current, 110 pA; scale bar, 10 nm) showing on-surface synthesized PA on Cu(110). **b**, A magnified STM image (bias voltage, 70 mV; current, 10 pA; scale bar, 2 nm) with blue and white ellipses indicating *cis*- and *trans*-PA chains, respectively. **c**, An nc-AFM image (bias voltage, 2 mV; oscillation amplitude, 70 pm; scale bar, 1 nm) revealing a mixture of *cis*- and *trans*-PA segments. **d**, From top to bottom: an nc-AFM image (bias voltage: 5 mV; oscillation amplitude, 70 pm), an STM image (bias voltage, 5 mV; current, 10 pA; scale bar, 0.5 nm), top- and side-view DFT models, and a simulated STM image of a *cis*-PA segment.

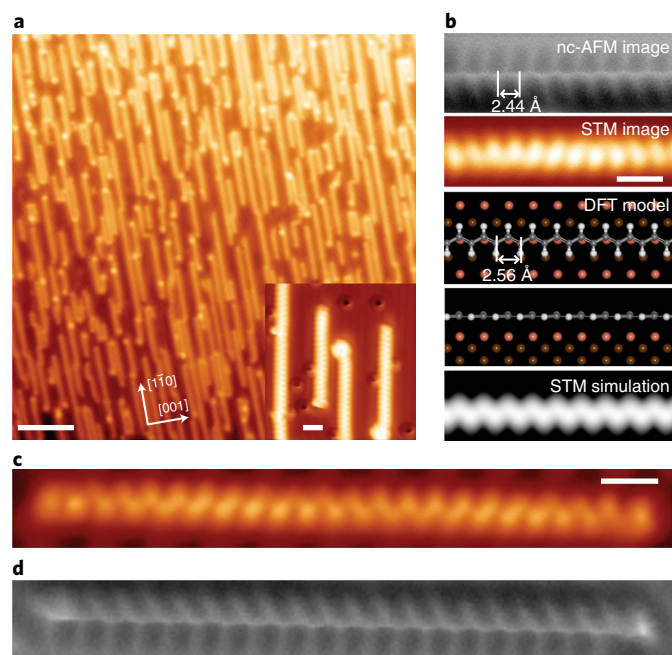


Fig. 3 | The structural properties of *trans*-PA. **a**, A large-scale STM image (bias voltage, -0.2 V; current, 10 pA; scale bar, 5 nm) showing pure *trans*-PA after annealing the sample to 470 K. The inset shows a high-resolution STM image (bias voltage, 5 mV; current, 10 pA; scale bar, 1 nm). **b**, From top to bottom: an nc-AFM image (bias voltage, 2 mV; oscillation amplitude, 70 pm; scale bar, 0.5 nm), an STM image (bias voltage, 5 mV; current, 10 pA), top- and side-view DFT models, and a simulated STM image of a *trans*-PA segment. **c**, An STM current image (bias voltage, 2 mV) of a 22-unit-long *trans*-PA oligomer. A moiré pattern is observed in **c** due to the lattice mismatch between *trans*-PA and Cu(110). **d**, An nc-AFM image (bias voltage, 2 mV; oscillation amplitude, 70 pm; scale bar, 0.5 nm) of the same chain in **c**.

Supplementary Fig. 7). At 0.75 eV binding energy (the middle panel of Fig. 4c), two straight lines along the [001] direction are observed, which split into four lines towards higher and lower energies

(see the left and right panels of Fig. 4c, respectively). Figure 4d displays the extracted band dispersion of *trans*-PA/Cu(110) along the $[1\bar{1}0]$ direction. We find two bands that cross at around 0.8 eV, a feature that is absent from the clean Cu(110) sample (see Supplementary Fig. 7). We assign these two bands to the π and π^* bands of *trans*-PA that originate from the even (π) and odd (π^*) parity of the wavefunction on neighbouring carbon atoms. This assignment directly implies complete closure of the band gap of Cu-supported *trans*-PAs; that is, a semiconductor-to-metal transition occurs following PA adsorption onto Cu(110). We investigated the effect of the heterogeneous chain length on the ARPES measurements (see Supplementary Figs. 8 and 9), where a dispersion relation that is compatible with the experiment is achieved considering a length distribution peaking around 5 nm.

The metallic nature of highly doped bulk *trans*-PA films has not been well understood^{13,14,19,36}. For the regime of high doping, it has been proposed that neighbouring soliton wavefunctions overlap, which results in a closing of the Peierls energy gap¹⁹. However, this idea encountered difficulties in explaining the observed localized infrared-active vibrational modes in halogen-doped *trans*-PA films¹⁴. To resolve this inconsistency, Park and co-workers proposed a soliton–antisoliton condensation picture¹³ that can explain both the metallic conductivity and the infrared-active vibrational modes in uniform halogen-doped *trans*-PA films. Aside from the uniform doping picture, theoretical models that consider disordered dopants—such as the random-dimer model³⁷—have also been proposed to explain the observed infrared-active vibrational modes. Our ARPES measurements indicate that homogeneous doping (here by the atomically flat single crystalline metal substrate) could indeed induce a closing in the Peierls energy gap of PA. We deduce an electron doping of 0.1 electrons per carbon atom from the shift of the charge neutrality point by Cu-substrate-induced doping by assuming completely linear bands: at charge neutrality (that is, one electron per carbon atom), the π band occupies 2.45 \AA^{-1} in reciprocal space, whereas electron doping by the Cu substrate (the charge neutrality point shifts from 0 to 0.8 eV binding energy as determined by ARPES measurements) changes the filled band occupation to 2.695 \AA^{-1} in reciprocal space. Therefore, the observed downshift of the π band is due to $2.695/2.45 = 1.10$ electrons per atom following doping; that is, an excess of 0.1 electrons per atom. This is well above the 0.05-electrons-per-carbon-atom doping level at which the

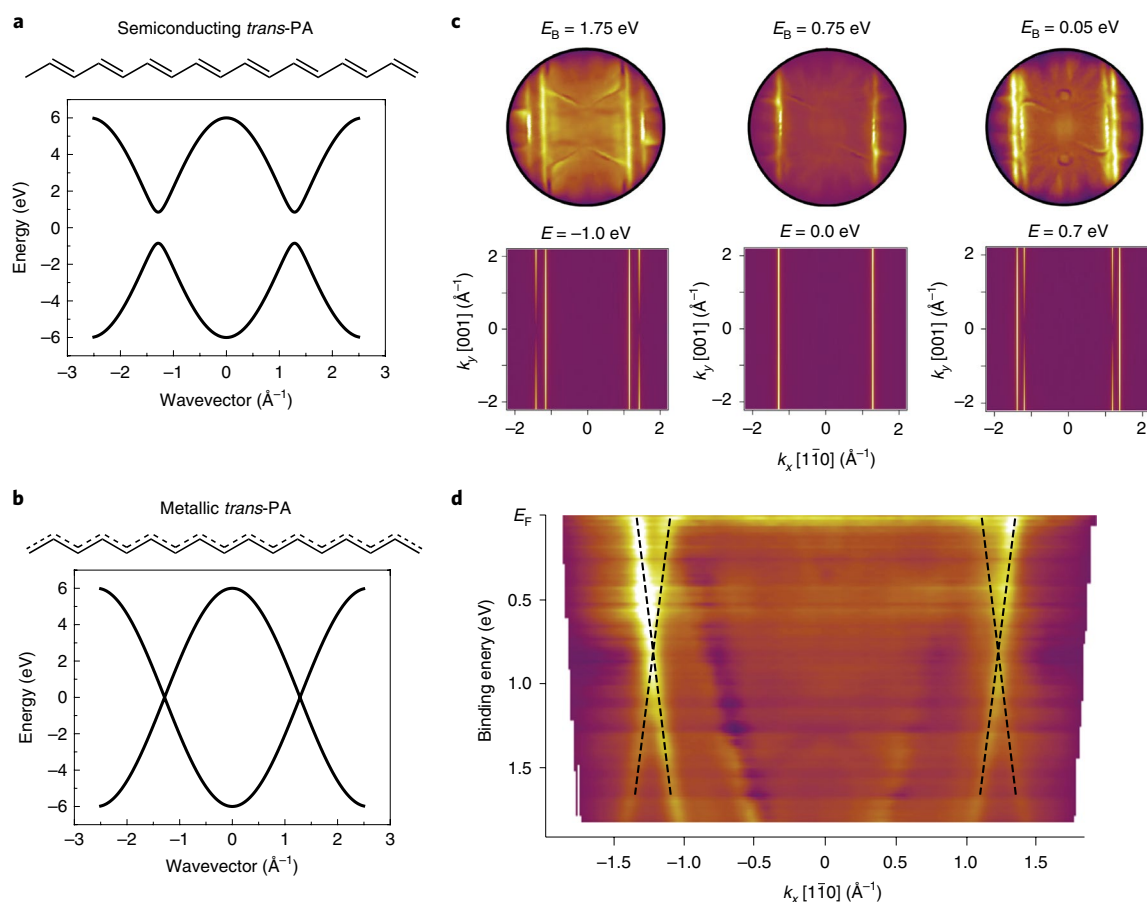


Fig. 4 | The band structure of *trans*-PA on Cu(110). **a,b**, Tight-binding-calculated band structures of semiconducting (**a**) and metallic (**b**) *trans*-PA. Suppression of the Peierls instability induces a semiconductor-to-metal transition. **c**, The constant-energy (top) and tight-binding-calculated (bottom) ARPES maps for a 40-dimer-long PA oligomer are shown. The maps show the photoemission intensity of the *trans*-PA-covered Cu(110) from which a map of a clean Cu(110) substrate has been subtracted. E_B is the binding energy. **d**, An $E(k)$ -map of the *trans*-PA/Cu(110) minus the clean Cu(110) along the $[1\bar{1}0]$ direction from ARPES measurements. The dashed lines are tight-binding-calculated bands. E_F indicates the Fermi level.

gap closure and the concomitant suppression of the Peierls bond length alternation are predicted to occur¹⁹. The Cu-substrate-doped *trans*-PA thus behaves similar to a 1D metal, which is consistent with the featureless local density of states seen in STS (see details in Supplementary Fig. 10). By contrast, we performed STS on *cis*-PAs, which shows an energy gap of 1.2 eV (see Supplementary Fig. 11). However, to clarify the debates on bulk *trans*-PA materials with inhomogeneous doping, further experiments will be needed that require synthesis or transfer of *trans*-PA on insulating substrates to access its intrinsic electronic properties, followed by deliberately introducing randomly distributed dopants.

To suppress the strong charge transfer doping, we tried to electronically decouple *trans*-PA from the underlying metal substrate by intercalating Cu oxide between *trans*-PA and the Cu(110) surface. As can be seen in Fig. 5a, after dosing oxygen molecules onto the sample kept at ~ 420 K, some *trans*-PA chains exhibited a higher apparent height than the others (marked by white dashed ellipses in Fig. 5a). We have verified that these chains are still structurally intact *trans*-PA chains (see details in Supplementary Figs. 12 and 13). The magnified STM image in Fig. 5b reveals that the PA segments with higher contrast have a periodicity of 5.0 Å, which corresponds to the Cu–Cu distance along the $[1\bar{1}0]$ direction of the oxygen reconstructed Cu(110)-(2 × 1)O substrate. This implies that the *trans*-PA segments with a higher apparent height adsorb on Cu(110)-(2 × 1)O, and they are thus expected to be electronically decoupled from the metal substrate. This assignment has been confirmed by STS

differential conductance (dI/dV) spectroscopy, where I denotes the tunneling current and V the bias voltage. The bottom panel of Fig. 5b displays dI/dV spectra taken at a decoupled *trans*-PA segment (red) and at a Cu-supported PA segment (black). The dI/dV spectrum taken on the Cu-supported *trans*-PA segment does not display any resonance peaks in the energy window from -2 to 1.5 eV due to the metallic nature of Cu-supported *trans*-PAs, and exhibits an overall shape in excellent agreement with the tight-binding-calculated density of states for metallic *trans*-PA (see Supplementary Fig. 10). By contrast, the decoupled *trans*-PA segment reveals two resonance peaks at -1.5 V and 0.9 V in the dI/dV spectrum, indicating an energy gap of $\Delta = 2.4$ eV. It is known that the band gap of *trans*-PA depends crucially on its bond length alternation pattern (that is, Peierls distortion). The value of $\Delta = 2.4$ eV determined by STS agrees well with the quasi-particle band gap of *trans*-PA (2.6 eV) for single/double C–C bond lengths of 1.45/1.34 Å (ref. 38). The DFT calculations for Cu- and oxide-supported *trans*-PA chains agree very well with our observations (see details in the Supplementary Fig. 5). For Cu-supported *trans*-PA, a strong hybridization of the *trans*-PA orbitals with the Cu(110) substrate is observed, which closes the DFT gap of the PA chain. For the oxide-supported *trans*-PA chain, however, the hybridization is weak and a DFT gap of 0.65 eV is evident. We notice that *trans*-PA chains will break into small hydrocarbon clusters or oxidized hydrocarbons after exposure to oxygen with a Cu substrate temperature higher than 450 K (see Supplementary Fig. 14).

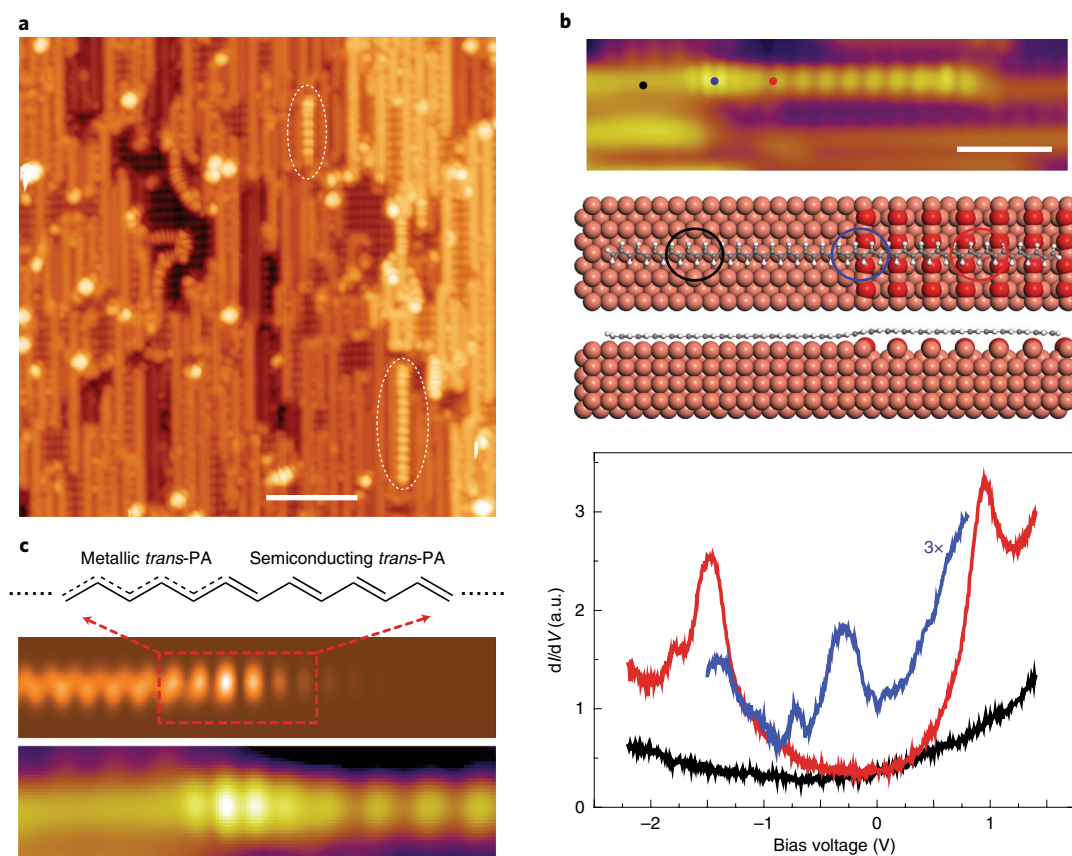


Fig. 5 | The electronic properties of decoupled *trans*-PA. **a**, An STM image (bias voltage, -1 V; current, 50 pA; scale bar, 5 nm) of *trans*-PA on Cu(110) after oxygen exposure. A few *trans*-PA segments are located on Cu(110)-(2 \times 1)O, showing a higher apparent height (marked by white dashed ellipses) than the others. **b**, From top to bottom: an STM image (bias voltage, -10 mV; current, 30 pA; scale bar, 1 nm), a top-view DFT-optimized structural model (the red spheres represent oxygen atoms) of a partially decoupled *trans*-PA with the circles indicating the regions of PA on Cu (black), at the Cu/oxide interface (blue) and on the oxide (red); a side-view DFT model; and a STS dI/dV spectra taken at the positions marked by coloured dots in the top STM image. **c**, The chemical structure of the interface between metallic *trans*-PA and semiconducting *trans*-PA (top); a tight-binding-calculated local density of states plot of the soliton-like interface state (middle) and an STM image (bias voltage, -10 mV; current, 30 pA) of the partially decoupled *trans*-PA segment (bottom).

Interestingly, we find that a mid-gap state emerges at the interface between the oxide- and the metal-supported *trans*-PA segments (see Fig. 5b, the blue spectrum). Tight-binding calculations suggest that this mid-gap state can be understood as an interface state between a semiconducting (oxide-supported) and a metallic (Cu-supported) *trans*-PA segment. The tight-binding-calculated local density of states plot of the interface state nicely agrees with our experimental observations (see Fig. 5c). We notice that the observed interface state is strongly localized to ~ 1 nm at the interface. We attribute this localization to the large band gap of *trans*-PA. The tight-binding calculations for a soliton state at the domain boundary between the two bond length alternation patterns of *trans*-PA reveal that its degree of localization depends crucially on the band gap of *trans*-PA, with the mid-gap soliton state becoming more and more localized with increasing band gap (see Supplementary Fig. 15).

Conclusions

We have demonstrated the successful bottom-up synthesis of atomically precise, individual PA chains on a Cu(110) substrate. Electronic decoupling of the PA from the metal substrate via Cu oxide intercalation reveals a band gap of 2.4 eV for *trans*-PA on Cu(110)-(2 \times 1)O, which is consistent with the intrinsic semiconducting nature of *trans*-PA. For the Cu-supported *trans*-PA, however, ARPES measurements reveal strong n-doping, which results in an energy gap closing by suppression of the Peierls bond length alternation. This

observation is nicely reproduced by tight binding calculations considering a uniform C–C bond length. A mid-gap state localized at the interface between the decoupled and Cu-supported segments has also been observed, originating from a semiconductor-to-metal transition at the interface. Our study provides a new platform for understanding the structural and electronic properties of *trans*-PA in real space, opening up many opportunities for further exploration of *trans*-PA and its derivatives. In particular, the direct synthesis of PA on more inert substrates will be helpful to observe the nature of intrinsic solitons at the domain walls between different phases of the bond length alternation pattern and to clarify the related controversial issues³⁵.

Methods

A commercial low-temperature STM/AFM (Scienta Omicron) was used for sample preparation and in situ characterization under ultrahigh vacuum conditions (with a base pressure below 1×10^{-10} mbar). The Cu(110) single crystal was cleaned by standard argon sputtering and annealing cycles. Acetylene molecules were dosed into the ultrahigh vacuum chamber through a leak valve with a typical pressure of 5×10^{-8} mbar for 5 min. The oxygen molecules were dosed at the PA/Cu(110) sample held at 200 °C through a leak valve with a pressure of 5×10^{-6} mbar for 30 min. The STM images were recorded in constant-current mode, and the dI/dV spectra were recorded using the lock-in technique with a small voltage modulation ($U_{r.m.s.} = 20$ mV). The nc-AFM images were recorded with a CO-functionalized tip attached to a quartz tuning fork sensor (with a resonance frequency of 3.5 kHz). The ARPES measurements were carried out in a laboratory photoemission spectroscopy (PES) system coupled to the

low-temperature STM/AFM, which allowed STM characterization of the sample before and after ARPES measurements. A FOCUS HIS 13 gas discharge lamp with a focusing mirror was used as excitation source delivering He(I) radiation of 21.2 eV. The PES data were measured using a VG Scienta R3000 XPS/UPS/ARPES electron analyser (where UPS is ultraviolet photoelectron spectroscopy) operated in the A20 angle-resolving lens mode with pass energy of 20 eV. In the fixed mode, $\pm 10^\circ$ and 2 eV photoemission intensity maps were acquired over the full hemisphere above the sample and stitched together to yield a full $I(\phi_{\text{azi}}, \theta_{\text{pol}}, E_{\text{kin}})$ three-dimensional ARPES data block with the kinetic energy measured with respect to the Fermi level, where ϕ_{azi} is the azimuth angle, θ_{pol} the polar angle and E_{kin} the kinetic energy. The raw data were twofold averaged according to the symmetry of the substrate. The conversion to k -space (k_x, k_y) was performed using the usual relations: $|k| = 1/h\sqrt{2m_e(E_{\text{kin}} - \text{WF})}$, $k_x = \sin(\phi_{\text{azi}})\cos(\theta_{\text{pol}})|k|$ and $k_y = \sin(\phi_{\text{azi}})\sin(\theta_{\text{pol}})|k|$, assuming a work function (WF) of 4.5 eV (h is Planck's constant, and m_e is the electron rest mass). The XPS measurements were performed at the Catalysis and Surface Science Endstation at the BL11U beamline in the National Synchrotron Radiation Laboratory. All of the core level spectra (including C 1s and Cu 2p) were recorded with a VG Scienta R4000 analyser using a monochromatic Al K α X-ray source. The peak fitting was performed using the XPS Peak 41 program with Gaussian functions after subtraction of a Shirley background.

The structural optimizations of PA on the surface were performed in the framework of DFT calculations by using the Vienna ab initio simulation package. We used the projector augmented-wave method^{39,40} and the Perdew–Burke–Ernzerhof generalized gradient approximation exchange–correlation functional⁴¹. Van der Waals interactions were included using Grimme's semi-empirical method (DFT-D3)⁴². The atomic structure was relaxed using the conjugate gradient algorithm scheme as implemented in Vienna ab initio simulation package until the forces on all unconstrained atoms were ≤ 0.01 eV \AA^{-1} .

The tight-binding simulation of the STM images were carried out in the C 2p_z orbital description with a nearest-neighbour hopping term ($\gamma_0 = 3$ eV), leading to the following Hamiltonian:

$$H = \sum_i \epsilon_0 c_i^+ c_i^- + \sum_{S < i, j >} -(\gamma_0 - \Delta\epsilon) c_j^+ c_i^- + \sum_{D < i, j >} -(\gamma_0 + \Delta\epsilon) c_j^+ c_i^-$$

with ϵ_0 conveniently set to zero and c_i^+ and c_i^- denoting the usual creation and annihilation operators on the atomic site i ; $S < i, j >$ denotes the sum over single-bond nearest neighbours and $D < i, j >$ the sum over double-bond nearest neighbours. Accordingly, $\Delta\epsilon$ represents the weakening/strengthening of the single/double bond. For $\Delta\epsilon = 0$ eV, the metallic solution of the non-dimerized PA chain is obtained, and for $\Delta\epsilon > 0$ eV, the solution will produce an energy gap of $4 \times \Delta\epsilon$. Numerically solving the model Hamiltonian yields the energy eigenvalues ϵ_i and the corresponding eigenstates α_{ij} (amplitude of state i on site j) from which the wave functions are computed assuming Slater-type atomic orbitals:

$$\psi_i(\mathbf{r}) = \sum_j \alpha_{ij} \times (z - z_j) \exp(-\zeta|\mathbf{r} - \mathbf{r}_j|)$$

where $\zeta = 1.625$ a.u. for the carbon 2p_z orbital. The charge density map $\rho(x, y)$ for a given energy range $[\epsilon_{\text{min}}, \epsilon_{\text{max}}]$ and height z_0 is then obtained by summing up the squared wave functions in this chosen energy range:

$$\rho(x, y) = \sum_{i, \epsilon_i \in [\epsilon_{\text{min}}, \epsilon_{\text{max}}]} \psi_i^2(x, y, z_0)$$

For the tight-binding simulations the atomic structure of the *trans*-PA was considered to have a C–C bond length of 1.41 \AA and a bond angle of 120° regardless of the single/double bond configuration and strength. Constant-charge density maps are taken as a first approximation to compare with experimental STM images.

Data availability

The datasets generated and/or analysed during the current study are available from the corresponding author on reasonable request.

Code availability

The tight-binding calculations were performed using a custom-made code on the WaveMetrics IGOR Pro platform. Details of this tight-binding code can be obtained from the corresponding author on reasonable request.

Received: 15 July 2018; Accepted: 24 July 2019;

Published online: 2 September 2019

References

- Chiang, C. K. Electrical conductivity in doped polyacetylene. *Phys. Rev. Lett.* **39**, 1098–1101 (1977).
- Shirakawa, H., Louis, E. J., MacDiarmid, A. G., Chiang, C. K. & Heeger, A. J. Synthesis of electrically conducting organic polymers: halogen derivatives of polyacetylene, (CH)_x. *J. Chem. Soc. Chem. Commun.* 578–580 (1977).
- Hsu, S. L., Signorelli, A. J., Pez, G. P. & Baughman, R. H. Highly conducting iodine derivatives of polyacetylene: raman, XPS and X-ray diffraction studies. *J. Chem. Phys.* **69**, 106–111 (1978).
- Heeger, A. J. Nobel lecture: semiconducting and metallic polymers: the fourth generation of polymeric materials. *Rev. Mod. Phys.* **73**, 681–700 (2001).
- Chiang, C. K. et al. Conducting polymers: halogen doped polyacetylene. *J. Chem. Phys.* **69**, 5098–5104 (1978).
- Fincher, C. R. et al. Electronic structure of polyacetylene: optical and infrared studies of undoped semiconducting (CH)_x and heavily doped metallic (CH)_x. *Phys. Rev. B* **20**, 1589–1602 (1979).
- Park, Y.-W., Heeger, A. J., Drury, M. A. & MacDiarmid, A. G. Electrical transport in doped polyacetylene. *J. Chem. Phys.* **73**, 946–957 (1980).
- Ikehata, S. et al. Solitons in polyacetylene: magnetic susceptibility. *Phys. Rev. Lett.* **45**, 1123–1126 (1980).
- Harada, I., Furukawa, Y., Tasumi, M., Shirakawa, H. & Ikeda, S. Spectroscopic studies on doped polyacetylene and β -carotene. *J. Chem. Phys.* **73**, 4746–4757 (1980).
- Ritsko, J. J. Core excitons in polyacetylene: evidence for a closed-gap metallic state. *Phys. Rev. Lett.* **46**, 849–852 (1981).
- Park, Y. W., Han, W. K., Choi, C. H. & Shirakawa, H. Metallic nature of heavily doped polyacetylene derivatives: thermopower. *Phys. Rev. B* **30**, 5847–5851 (1984).
- Park, Y. W. et al. Electrical conductivity of highly-oriented-polyacetylene. *Solid State Commun.* **65**, 147–150 (1988).
- Park, Y. W., Yoon, C. O., Na, B. C., Shirakawa, H. & Akagi, K. Metallic properties of transition metal halides doped polyacetylene: the soliton liquid state. *Synth. Met.* **41**, 27–32 (1991).
- Lavarda, F. C., Galvo, D. S. & Laks, B. Extended states in finite one-dimensional, disordered, highly doped, ItransR-polyacetylene chains. *Phys. Rev. B* **45**, 3107–3110 (1992).
- Shirakawa, H. The discovery of polyacetylene—the dawning of an era of conducting polymers. *Curr. Appl. Phys.* **1**, 281–286 (2001).
- Heeger, A. J. Semiconducting and metallic polymers: the fourth generation of polymeric materials. *J. Phys. Chem. B* **105**, 8475–8491 (2001).
- Su, W. P., Schrieffer, J. R. & Heeger, A. J. Solitons in polyacetylene. *Phys. Rev. Lett.* **42**, 1698–1701 (1979).
- Heeger, A. J., Kivelson, S., Schrieffer, J. R. & Su, W.-P. Solitons in conducting polymers. *Rev. Mod. Phys.* **60**, 781–850 (1988).
- Mele, E. J. & Rice, M. J. Semiconductor-metal transition in doped polyacetylene. *Phys. Rev. B* **23**, 5397–5412 (1981).
- Lavarda, F. C., dos Santos, M. C., Galvão, D. S. & Laks, B. Insulator-to-metal transition in polythiophene. *Phys. Rev. B* **49**, 979–983 (1994).
- Grill, L. et al. Nano-architectures by covalent assembly of molecular building blocks. *Nat. Nanotechnol.* **2**, 687–691 (2007).
- Zhong, D. et al. Linear alkane polymerization on a gold surface. *Science* **334**, 213–216 (2011).
- Cai, J. et al. Atomically precise bottom-up fabrication of graphene nanoribbons. *Nature* **466**, 470–473 (2010).
- Ruffieux, P. et al. On-surface synthesis of graphene nanoribbons with zigzag edge topology. *Nature* **531**, 489–492 (2016).
- Pavliček, N. et al. Synthesis and characterization of triangulene. *Nat. Nanotechnol.* **12**, 308–311 (2017).
- Zhang, Y.-Q. et al. Homo-coupling of terminal alkynes on a noble metal surface. *Nat. Commun.* **3**, 1286 (2012).
- Liu, J. et al. Lattice-directed formation of covalent and organometallic molecular wires by terminal alkynes on Ag surfaces. *ACS Nano* **9**, 6305–6314 (2015).
- Sun, Q. et al. Bottom-Up synthesis of metalated carbyne. *J. Am. Chem. Soc.* **138**, 1106–1109 (2016).
- Zhou, H. et al. Direct visualization of surface-assisted two-dimensional diyne polycyclotrimerization. *J. Am. Chem. Soc.* **136**, 5567–5570 (2014).
- Liu, J., Ruffieux, P., Feng, X., Müllen, K. & Fasel, R. Cyclotrimerization of arylalkynes on Au(111). *Chem Commun.* **50**, 11200–11203 (2014).
- Lomas, J. R., Baddeley, C. J., Tikhov, M. S. & Lambert, R. M. Ethyne cyclization to benzene over Cu(110). *Langmuir* **11**, 3048–3053 (1995).
- Gross, L., Mohn, F., Moll, N., Liljeroth, P. & Meyer, G. The chemical structure of a molecule resolved by atomic force microscopy. *Science* **325**, 1110–1114 (2009).
- Barborini, M. & Guidoni, L. Ground state geometries of polyacetylene chains from many-particle quantum mechanics. *J. Chem. Theory Comput.* **11**, 4109–4118 (2015).
- Natta, G., Mazzanti, G. & Corradini, P. in *Stereoregular Polymers and Stereospecific Polymerizations* 463–465 (Pergamon, 1967); <https://doi.org/10.1016/B978-1-4831-9883-5.50084-2>
- Hudson, S. B. Polyacetylene: myth and reality. *Materials* **11**, 242–261 (2018).
- Chien, J. C. W., Warakomski, J. M., Karasz, F. E., Chia, W. L. & Lilla, C. P. Homogeneous doping and semiconductor-to-“metal” transition in polyacetylene. *Phys. Rev. B* **28**, 6937–6952 (1983).

37. Dunlap, D. H., Wu, H.-L. & Phillips, P. W. Absence of localization in a random-dimer model. *Phys. Rev. Lett.* **65**, 88–91 (1990).
38. Ferretti, A. et al. Ab initio complex band structure of conjugated polymers: effects of hybrid density functional theory and GW schemes. *Phys. Rev. B* **85**, 235105 (2012).
39. Kresse, G. & Joubert, D. From ultrasoft pseudopotentials to the projector augmented-wave method. *Phys. Rev. B* **59**, 1758–1775 (1999).
40. Blöchl, P. E. Projector augmented-wave method. *Phys. Rev. B* **50**, 17953–17979 (1994).
41. Perdew, J. P., Burke, K. & Ernzerhof, M. Generalized gradient approximation made simple. *Phys. Rev. Lett.* **77**, 3865–3868 (1996).
42. Grimme, S., Antony, J., Ehrlich, S. & Krieg, H. A consistent and accurate ab initio parametrization of density functional dispersion correction (DFT-D) for the 94 elements H–Pu. *J. Chem. Phys.* **132**, 154104 (2010).

Acknowledgements

This work was supported by the Swiss National Science Foundation, the European Union's Horizon 2020 research and innovation programme under grant agreement no. 785219 (Graphene Flagship Core 2), and the Office of Naval Research BRC programme. W.X. acknowledges financial support from the National Natural Science Foundation of China (grant nos. 21473123, 21622307, 21790351). S.W. acknowledges financial support from Thousand Young Talent Program and National Natural Science Foundation

of China (grant nos. 11874258, 11790313). C.A.P. acknowledges the Swiss National Supercomputing Centre (CSCS) under project ID s746.

Author contributions

W.X., R.F. and P.R. conceived the experiments. Q.S., S.W. and L.C. performed the STM experiments. S.W., B.Y., C.L. and X.Y. performed nc-AFM and STS measurements. R.W., S.W. and O.G. performed the ARPES experiments. Q.S., O.G. and C.A.P. performed the calculations. H.J., Q.S., X.Y. and J.Z. performed the XPS experiments. S.W., Q.S., R.F. and W.X. wrote the paper. All authors discussed the results and implications and commented on the manuscript at all stages.

Competing interests

The authors declare no competing financial interests.

Additional information

Supplementary information is available for this paper at <https://doi.org/10.1038/s41557-019-0316-8>.

Reprints and permissions information is available at www.nature.com/reprints.

Correspondence and requests for materials should be addressed to R.F. or W.X.

Publisher's note: Springer Nature remains neutral with regard to jurisdictional claims in published maps and institutional affiliations.

© The Author(s), under exclusive licence to Springer Nature Limited 2019